This is the peer-reviewed, final accepted version for American Mineralogist, published by the Mineralogical Society of America.
The published version is subject to change. Cite as Authors (Year) Title. American Mineralogist, in press.
DOI: https://doi.org/10.2138/am-2021-7696. http://www.minsocam.org/

Revision 1

Three-dimensional and microstructural fingerprinting of gold nanoparticles at fluid-mineral interfaces

HAOYANG ZHOU[1]*, RICHARD WIRTH[1], SARAH A. GLEESON[1,2], ANJA SCHREIBER[1], AND SATHISH MAYANNA[1]

[1]*GFZ German Research Centre for Geosciences, Telegrafenberg, Potsdam 14473, Germany*

[2]*Institute of Geological Sciences, Freie Universität Berlin, Berlin 12249, Germany*

*Present address: Natural History Museum, University of Oslo, P.O. Box 1172, Blindern, 0318 Oslo, Norway. E-mail: hzhou@gfz-potsdam.de; haoyang.zhou@nhm.uio.no

ABSTRACT

Recent studies have identified gold nanoparticles in ores in a range of deposit types but little is known about their formation processes. In this contribution, gold-bearing magnetite from the well-documented, world-class, Beiya Au deposit, China was investigated in terms of microstructure and crystallography at the nanoscale. We present the first three-dimensional (3D) focused ion beam/scanning electron microscopy (FIB/SEM) tomography of the distribution of gold nanoparticles in nanopores in the low-Si magnetite. The porous low-Si magnetite, which overprints an earlier generation of silician magnetite, was formed by a coupled dissolution-reprecipitation reaction (CDRR). The extrinsic changes in thermodynamic conditions (e.g., S content and temperature) of the hydrothermal fluids resulted in the CDRR in magnetite and the disequilibrium of Au-Bi melts. The gold nanoparticles crystallized from Au-supersaturated fluids originating from the disequilibrium of Au-Bi melts and grew in two ways depending on the intrinsic crystal structure and pore textures: 1) heteroepitaxial growth utilizing the (111) lattice

planes of magnetite, and 2) randomly oriented nucleation and growth. Therefore, this study unravels how intrinsic and extrinsic factors drove the formation of gold nanoparticles at fluid-mineral interfaces.

Keywords: Gold nanoparticle, nanopore, fluid-mineral interface, 3D FIB/SEM tomography, microstructure, coupled dissolution-reprecipitation reaction

INTRODUCTION

Some of the largest Au deposits in the world contain high-grade ores of "invisible" gold (e.g., Carlin-type deposits; Cook and Chryssoulis, 1990; Simon et al., 1999b). Based on in-situ trace element, spectroscopic and experimental analyses, it has been suggested that "invisible" gold is often present in the lattice of the ore minerals such as (arsenian) pyrite (Simon et al., 1999a; Reich et al., 2005) and that the partitioning of Au is a function of the As content of the pyrite (Kusebauch et al., 2019; Xing et al., 2019). The final uptake of Au by the pyrite lattice also depends on complex intrinsic (e.g., crystal surface structure, heteroepitaxial growth, and diffusion-limited self-organization) and extrinsic factors (e.g., pressure; Wu et al., 2019).

Recent advances in imaging by transmission electron microscopy (TEM) have shown that "invisible" gold can also exist as nanoparticles in the ore minerals (Palenik et al., 2004; Reich et al., 2006; Ciobanu et al., 2012). Multiple models for the formation of gold nanoparticles in high-temperature systems have been suggested including gold exsolution from solid solution (Palenik et al., 2004), gold saturation during sulfide precipitation (Reich et al., 2005) and gold precipitation from pore-attached vapors (Ciobanu et al., 2012). However, it can be difficult to discriminate between these models because the textural association of gold nanoparticles with the host minerals is hard to characterize at the nanoscale, and is sometimes ambiguous based on two-dimensional (2D) textural analysis (e.g., Godel et al., 2010). Recently, 3D analysis using

atom probe tomography (APT) interpreted gold nanoparticles as a growth feature, being formed via the diffusion of Au atoms on surfaces of slow-growing sulfides (Fougerouse et al., 2016). Therefore, further investigation of the gold nanoparticles in the ore minerals is required to understand the formation processes at fluid-mineral interfaces, especially utilizing high-resolution and 3D imaging techniques.

The focused ion beam/scanning electron microscopy (FIB/SEM) tomography, also known as FIB/SEM slice and view technology, is a novel and powerful tool for 3D analysis via serial FIB slicing the material followed by SEM imaging. It offers great advantages in both morphological characterization and spatial resolution (down to a few nanometers) and so can be used to characterize the micro- to nanoscale microstructural features of geomaterials (Wirth, 2009). Therefore, a combination of high-resolution FIB-based 3D SEM tomography and TEM analysis, was used in this study to investigate magnetite containing abundant gold particles from the world-class Beiya Au deposit, Southwest China (Zhou et al., 2017). Integrating the high-resolution 3D distribution and the crystallographic relationship of gold nanoparticles and nanopores in magnetite, we examine the fluid-mineral interfacial processes responsible for the formation of gold nanoparticles.

SAMPLE BACKGROUND AND DESCRIPTION

The ~36 Ma-old Beiya polymetallic Au deposit in the eastern Jinshajiang fault zone of the eastern Tibetan plateau contains 11.9 million ounces of Au at a grade of 2.52 g/t and is the third-largest Au deposit in China (Fig. 1; Mao et al., 2017; Zhou et al., 2019). The main mineralization occurs as a skarn and is divided into prograde- and retrograde- stages. The latter is auriferous and can be subdivided into oxide- (magnetite-dominated) and sulfide- (pyrite- and chalcopyrite-dominated) stages (Zhou et al., 2016, 2017). At least 14% of the total Au endowment is hosted

by magnetite but it is not currently extracted (Zhou et al., 2017). From the oxide to sulfide stages, the ore-forming fluids evolved from hypersaline, high temperature (~360–510 °C) to lower salinity, lower temperature (~165–350 °C) conditions, which is attributed to the ingress of meteoric water into the magmatic system (He et al., 2017).

Two magnetite gold ores (Au-1 and Au-2) sampled from the Beiya deposit were used in this study. Au-1 comes from orebody KT52 (the largest Au orebody at Beiya) in the Wandongshan open-pit (E100°11′33″, N26°10′3″, 1630 m altitude), whereas Au-2 was collected from the drill core 56ZK23 at 402 m depth which crosscuts orebody KT57 (Fig. 1b). Au-1 consists of abundant magnetite, quartz, subordinate pyrite and chalcopyrite, while Au-2 is mainly composed of magnetite, pyrite, chalcopyrite, chlorite, biotite, siderite and quartz. The Au grades (fire assay) for Au-1 and Au-2 are 15.3 and 25.5 g/t, but a nugget effect cannot be ruled out as only small chips were assayed for each sample.

METHODOLOGY

FIB/SEM and TEM analyses were conducted at the German Research Centre for Geosciences, Potsdam, Germany (GFZ Potsdam). Eight magnetite foils (~ 15 × 10 × 0.15 μm for each) were cut from three polished thin sections with a FEI Helios G4 UC Dual Beam FIB using Ga ion source. The surfaces of interest were covered with thin, Pt-protective layers followed by sputtering material out in front and sides by Ga ions at a 30-kV voltage and a 47-nA current. The front side of each foil was subsequentially milled by Ga ions under a 2.5-nA current. All FIB foils were finally polished at 5 kV and 41 pA to remove re-deposited material. The detailed procedures of cutting a FIB foil were described by Wirth (2004, 2009). The FIB foils were fixed in the Cu-grids and were not carbon-coated. A FEI Tecnai G2 F20 X-Twin TEM, equipped with a high-angle annular dark-field (HAADF) detector and an energy-dispersive X-ray spectroscopy

(EDX), was employed to investigate the foils at a 200-kV voltage. The diffraction patterns (fast Fourier transformation, FFT) were calculated from the high-resolution lattice fringes images. The sizes and numbers of nanopores were measured using the software Image J.

Three-dimensional (3D) tomography in this study was based on the slice and view technology of the dual-beam (FIB/SEM) systems. After careful examination under the backscattered electron (BSE) mode and with EDX, a magnetite grain bearing only gold nanoparticles was selected. A 0.7-μm carbon-protective layer was coated on the surface of the region of interest. The front and lateral material of the target were removed by Ga ion sputtering to produce a cubic volume of ~15 × 15 × 15 μm^3. Based on the beam geometries in the dual-beam systems, the sample was tilted with an angle of 54°. The voltage and current were 5 kV and 50 nA for the electron beam and were 30 kV and 0.23 nA for the ion beam. An automatic protocol of slice-cutting followed by SEM-imaging on surface of cross-sections was applied to produce the FIB-SEM tomograms. The slice distance was set at 17.6 nm and a stack of 991 SEM images were obtained using an E-T detector. The 3D reconstruction was conducted with the software Avizo 7.0, but only the middle 600 SEM images were loaded to maximize the overlapping areas. Because of the low contrast of some nanopores to the background, the reconstructed results display locally high noise for nanopores. Except for this, the rendered nanopores basically match their distribution in the 2D SEM images.

RESULTS

Microstructure in magnetite

Two types of magnetite were defined in this study: silician and low-Si magnetite (Figs. 2 and 3). Specifically, silician magnetite is euhedral, nonporous and devoid of mineral inclusions. It shows oscillatory zoning in the BSE images (Fig. 2a) but has Si contents that can be measured

by EDX (Fig. 3b). In contrast, low-Si magnetite is brighter in the BSE images (Figs. 2a–2c) and has no detectable Si (Fig. 3b). It occurs as irregular domains within, or penetrating, through the silician magnetite (Figs. 2a–2c). Bright-field (BF) imaging across the interface of the two magnetite types shows that they have the same crystallographic orientation (like a single crystal; Fig. 2f). The low-Si magnetite is characterized by high porosity (Figs. 2a–2c), with a local mean pore size down to 5 nm (n = 1241; Figs. 4a and 4b); some nanopores have a rhombic morphology (Fig. 4a). In the 3D image, these nanopores are partially interconnected (Fig. 5; Video 1). The nanopores are empty (Fig. 6c) or filled with Si-bearing phases (Fig. 6d). Abundant nanometer-sized Au and Bi phases (e.g., native bismuth, maldonite, bismuthinite, galenobismutite and Bi-Pb-Ag sulfosalts) are present in the nanopores in low-Si magnetite, with the Bi phases dominated by Bi-sulfides and -sulfosalts (Figs. 3 and 7a).

Gold nanoparticles

Gold occurs as submicron- to nanometer-sized grains which can be as small as ~5 nm (Figs. 2–7; Video 2). Both 3D, HAADF and BF images show that gold nanoparticles are attached to nanopores in the low-Si magnetite (Figs. 2, 3, 5 and 6; Video 3). In the 2D images, the morphology of the gold nanoparticles is elongate (Fig. 6a), triangular (Fig. 2d) or hexagonal (Fig. 6f). In the 3D images, gold is present as octahedral or flat nanoparticles in the low-Si magnetite and interestingly, most flat gold nanoparticles are oriented (Fig. 5; Video 2). Clusters of gold nanoparticles can occur alone in a single grain of low-Si magnetite (Fig. 2b), but are always companied by nanoparticle assemblages of Bi phases (e.g., native bismuth, bismuthinite) several ten to hundreds of micrometers away (Fig. 2a). The gold nanoparticles have sharp contacts with native bismuth as well as maldonite (Figs. 7b and 7c). The high-resolution TEM (HRTEM) images display two distinct orientation types of the gold nanoparticles in the host

138 magnetite: 1) an orientation relationship, where (111) planes of gold are parallel to (111) planes
139 of magnetite (Fig. 6h), and 2) random orientation of gold grains (Fig. 6i). In the first case, the
140 gold nanoparticles are always elongate and occur along sub-grain boundaries (low-angle
141 boundaries) separated by defects in magnetite (Fig. 6g). In contrast, randomly oriented gold
142 nanoparticles are located along sub-grain boundaries of magnetite or within the magnetite sub-
143 grains.

144 ## DISCUSSION

145 In ore systems, gold nanoparticles can be found together with silica in hypogene ores
146 formed via colloidal processes (e.g., in epithermal and orogenic deposits) or occur in weathering
147 deposits resulting from supergene or bio-processes (Hough et al., 2011; Petrella et al., 2020).
148 Gold nanoparticles can be also present in refractory ores most commonly in As-bearing Fe-
149 sulfides, e.g., (arsenian) pyrite and arsenopyrite (Palenik et al., 2004; Reich et al., 2006).
150 Although Zhou et al. (2017) described submicron-sized gold particles in magnetite, their
151 morphology, and their mineralogical relationship to the magnetite, was ambiguous due to the
152 limited resolution of 2D SEM. Therefore, the mechanism by which the magnetite incorporated a
153 large number of gold particles was unknown. Here, we present the high-resolution TEM and 3D
154 morphological images of "invisible" gold in magnetite, which is the first application of the
155 FIB/SEM slice and view technology to the study of "invisible" gold in an ore mineral.

156 In 2D some of the gold nanoparticles appear to fully enclosed in magnetite but in fact are
157 linked to nanopores in the third dimension (Fig. 5c). The 3D image also displays that the
158 nanopores are interconnected to some extent (Fig. 5b), which suggests that they denote channels
159 of migrating fluids (e.g., Harlov et al., 2005; Birski et al., 2018). Therefore, we argue that the
160 gold nanoparticles were precipitated from a fluid phase, rather than non-fluid mediated

exsolution from the host low-Si magnetite.

Coupled dissolution-reprecipitation reaction making magnetite porous

The textural relationships suggest that the silician magnetite is replaced by the low-Si magnetite (Figs. 2a–2c). We note that 1) the late low-Si magnetite has high porosity, while the early silician magnetite is less porous; 2) the contacts are sharp between the two magnetite types; and 3) the same crystallographic orientation between the two magnetite types indicates a topotactic reaction, i.e., the orientation of the low-Si magnetite depends on that of the already existing silician magnetite. These are diagnostic features for the low-Si magnetite formed by a coupled dissolution-reprecipitation reaction (CDRR; Putnis et al., 2002; Altree-Williams et al., 2015). This is a fluid-mediated process that typically involves dissolution of a parent mineral (e.g., the silician magnetite) followed by reprecipitation of a stable product phase (e.g., the low-Si magnetite) at the reaction front (Putnis et al., 2002; Altree-Williams et al., 2015; Yin et al., 2019). Silician magnetite is of higher lattice energy relative to low-Si magnetite, so a fluid phase in disequilibrium with silician magnetite can dive the CDRR to decrease the Gibbs free energy of minerals finally (Putnis et al., 2002; Dubacq and Plunder, 2018).

In fact, there are studies documenting CDRR in magnetite in skarn systems which attribute the process to changes in oxygen fugacity (fO_2), temperature, salinity and pressure of the fluids (e.g., Hu et al., 2015). In the Beiya skarn ores, the newly-formed low-Si magnetite always occurs as irregular domains in the silician magnetite. The lack of an overgrowths of the low-Si magnetite on the silician magnetite suggests that the fluids responsible for CDRR probably did not cause significant new magnetite formation and the metals required for precipitation of the low-Si magnetite predominantly came from dissolution of the early silician magnetite. Given the abundant Bi-sulfide and -sulfosalt nanoparticles (e.g., bismuthinite, galenobismutite, Bi-Pb-Ag-S

184 phases) in the low-Si magnetite, we argue that the CDRR probably took place at the transition
185 from the oxide- to sulfide- stages during the evolution of the Beiya hydrothermal system. The
186 transition was caused by cooling and influx of meteoric water (He et al., 2017) and was
187 companied with changes in fluid thermodynamic conditions, e.g., a decrease in temperature,
188 salinity (He et al., 2017) and an increase in (reduced) S content (Seo et al., 2009). We suggest
189 that these thermodynamic changes gave rise to the dissolution of the silician magnetite followed
190 by supersaturation with respected to purer (low-Si) magnetite (Figs. 9a and 9b).

191 Formation of numerous pores in product minerals is an important feature for CDRR, which
192 results from volume reduction of the product phases and allows the propagation of reaction front
193 towards the parent minerals (Putnis, 2002; Ruiz-Agudo et al., 2014). We highlight that such a
194 porous texture offers critical spaces for the nucleation and growth of gold nanoparticles inside
195 the low-Si magnetite. For comparison, another FIB foil of the low-Si magnetite with few
196 nanopores is devoid of gold nanoparticles (Fig. 4c). Another expectation is that interconnectivity
197 of nanopores in the low-Si magnetite was reduced due to progressive reequilibration especially
198 behind the reaction front. Some nanopores may have been annealed out by fluids due to Ostwald
199 ripening (Ruiz-Agudo et al., 2014). This is consistent with the partially interconnected nanopores
200 revealed by the 3D FIB/SEM tomography.

201 **Growth of gold nanoparticles from Au-supersaturated fluids in nanopores**

202 The two observed orientation relationships between the gold nanoparticles and low-Si
203 magnetite represent two different nucleation and growth mechanisms for gold nanoparticles. The
204 parallel orientation relationship suggests the heteroepitaxial growth of elongate gold
205 nanoparticles on the low-Si magnetite surfaces. The d-spacing of (111) planes for gold is 2.36 Å,
206 approximately half of the d-spacing of (111) planes for magnetite (4.85 Å). In our case, the

measured d-spacings of the (111) planes for gold and host magnetite are 2.41 and 4.81 Å (Figs. 6h), supporting such a scenario. This growth pattern compensates the lattice mismatch between the two different solid phases and minimizes the lattice strain energy (Zheleva et al., 1994). Moreover, the (111) crystallographic plane of magnetite with the highest surface energy is where nucleation would happen preferentially (Jia and Gao, 2008). It has been suggested that if the contact angle of crystals (e.g., the gold nanoparticles) and the pore wall is small, the pore wall can be an effective nucleating agent (Scherer, 1999). In this case, gold nanoparticles would nucleate from the pore-fluids using the magnetite lattice parallel to the (111) lattice planes. This can explain the oriented alignment of the flat gold nanoparticles in the low-Si magnetite observed from the 3D images. The flat planes of the gold nanoparticles probably result from the preferential growth of the (111) lattice planes.

In contrast, the second type of gold nanoparticles had random orientation relationships with the magnetite indicating that they nucleated and grew with little or no contact with magnetite surfaces. This is because these pore walls are not favorable nucleation sites due to their large contact angles with the crystals (Scherer, 1999). Hence, the diversity of nucleation and growth orientation types resulted from intrinsic factors such as crystal structure and pore textures of gold and magnetite at fluid-mineral interfaces.

Immiscible Bi melts can directly fractionate and effectively collect (ionic) gold from coexisting fluids, forming Au-Bi melts (Tooth et al., 2008, 2011). In this study, rare nanometer-sized Au-Bi blebs of native bismuth + gold and native bismuth + maldonite have sharp contacts and are interpreted as eutectic alloys from nanometer-scaled Au-Bi melts (Figs. 7b–7c and 8). Although these Au-Bi blebs were found in the low-Si magnetite, their stability was not thermodynamically supported by the high reduced sulfur content for the hydrothermal fluids

responsible for CDRR (Zhou et al., 2017). As Bi commonly exists as trivalent oxidation state in the fluids (Tooth et al., 2011), the fractionation of Au-Bi melts from the hydrothermal fluids at Beiya has been thermodynamically attributed to an early decrease in fO_2 lower than the hematite-magnetite buffer (Zhou et al., 2017), which resulted in onset of magnetite crystallization. Given the overwhelming Bi-sulfides and sulfosalts over native bismuth or maldonite in the low-Si magnetite (Figs. 3b and 7a) and the replacement texture of the Au-Bi blebs by Bi-sulfides and sulfosalts (Figs. 7a and 7d), we suggest that these Au-Bi blebs represent the relicts of Au-Bi melts that should be coeval with the early silician magnetite (Fig. 9a). Although the Au-Bi melt droplets would have a high density, we argue that they were hardly separated from the fluids due to the high surface tension of the nanoparticles. Similar Bi melt droplets trapped in fluid inclusions have been found in an iron oxide copper-gold (IOCG) deposit (Acosta-Góngora et al., 2015). This, in turn, is favorable for Au refining by the suspended Bi melts, a process previously identified at Beiya (Zhou et al., 2017).

It is probable that the variations in thermodynamic conditions responsible for CDRR in magnetite also accounted for the disequilibrium of Au-Bi melts (Fig. 9b), given the accumulation of Bi-Au assemblages at the reaction front in magnetite (Fig. 3b). Thermodynamically, Bi^0 was converted to bismuthinite (or other Bi sulfides such as galenobismutite if Pb was present simultaneously) when temperature dropped and reduced S content increased (Zhou et al., 2017). The solubility of Au is extremely high in Bi melts (up to ~35 wt.% at 400 °C; Fig. 8) but is much lower in geological fluids (ppb-level; Williams-Jones et al., 2009). Nanoparticles are always formed from the supersaturated fluids where nucleation rates are much higher than growth rates (e.g., Hochella et al., 2008). Therefore, we argue that the disequilibrium of Au-Bi melts released

Au into fluids, resulting in the formation of local (pore-scale) Au-supersaturated fluids from which the gold nanoparticles in the low-Si magnetite crystallized (Fig. 9c).

IMPLICATIONS

Two generations of magnetite (non-porous silician and porous low-Si) are interpreted to result from CDRR at the ore stage in the world-class Beiya Au deposit, Southwest China. We have presented the first 3D FIB/SEM tomography of abundant gold nanoparticles in the nanopores of the low-Si magnetite. We argue that the gold nanoparticles crystallized from Au-supersaturated fluids which originated from the disequilibrium of Au-Bi melts. We illustrate the role of intrinsic (e.g., crystal structure and pore textures) and extrinsic factors (e.g., reduced S content and temperature) in the formation of gold nanoparticles at fluid-mineral interfaces.

Non-lattice-bound "invisible" gold in mineral deposits is commonly interpreted to be remobilized from exsolution of earlier formed minerals (e.g., Large et al., 2007; Sung et al., 2009; Cook et al., 2013). However, our work offers an alternative explanation in that this gold can be also introduced by later hydrothermal fluids during progressive mineralization. In addition, this study indicates that "invisible" gold nanoparticles in ore minerals, perhaps not solely in magnetite, may result from nano-scale permeability between nanopores developed from CDRR on earlier minerals.

ACKNOWLEDGMENTS

This work was financed by the National Natural Science Foundation of China (No. 91855213), the National Key Research and Development Program of China (No. 2018YFA0702605), and the National Key Basic Research Program of China (No. 2015CB452604). Sarah A. Gleeson and Sathish Mayanna acknowledge the financial support of

the Helmholtz Recruiting Initiative (No. 0316 and I-044-16-01 respectively). We are grateful to Denis Fougerouse and three anonymous reviewers for their critical comments on the manuscript.

REFERENCES CITED

Acosta-Góngora, P., Gleeson, S.A., Samson, I.M., and L. Ootes, L.C., 2015, Gold refining by bismuth melts in the iron oxide-dominated NICO Au-Co-Bi (±Cu±W) deposit, NWT, Canada: Economic Geology, v. 110, p. 291–314.

Altree-Williams, A., Pring, A., Ngothai, Y., and Brugger, J., 2015, Textural and compositional complexities resulting from coupled dissolution–reprecipitation reactions in geomaterials: Earth-Science Reviews, v. 150, p. 628–651.

Birski, Ł., Wirth, R., Słaby, E., Wudarska, A., Lepland, A., Hofmann, A., and Schreiber, A., 2018, (Ca-Y)-phosphate inclusions in apatite crystals from Archean rocks from the Barberton Greenstone Belt and Pilbara Craton: First report of natural occurrence: American Mineralogist, v. 103, p. 307–313.

Ciobanu, C.L., Cook, N.J., Utsunomiya, S., Kogagwa, M., Green, L., Gilbert, S., and Wade, B., 2012, Gold-telluride nanoparticles revealed in arsenic-free pyrite: American Mineralogist, v. 97, p. 1515–1518.

Cook, N.J., and Chryssoulis, S.L., 1990, Concentrations of invisible gold in the common sulfides: The Canadian Mineralogist, v. 28, p. 1–16.

Cook, N.J., Ciobanu, C.L., Meria, D., Silcock, D., and Wade, B., 2013, Arsenopyrite-pyrite association in an orogenic gold ore: Tracing mineralization history from textures and trace elements: Economic Geology, v. 108, p. 1273–1283.

Dubacq, B., and Plunder, A., 2018, Controls on trace element distribution in oxides and silicates: Journal of Petrology, v. 59, p. 233–256.

297 Fougerouse, D., Reddy, S.M., Saxey, D.W., Rickard, W.D.A., Riessen, A.V., and Micklethwaite,
298 S., 2016, Nanoscale gold clusters in arsenopyrite controlled by growth rate not concentration:
299 Evidence from atom probe microscopy: American Mineralogist, v. 101, p. 1916–1919.
300 Godel, B., Barnes, S.J., Barnes, S., and Maier, W.D., 2010, Platinum ore in three dimensions:
301 Insights from high-resolution X-ray computed tomography: Geology, v. 38, p. 1127–1130.
302 Harlov, D.E., Wirth, R., and Förster, H., 2005, An experimental study of dissolution–
303 reprecipitation in fluorapatite: fluid infiltration and the formation of monazite: Contributions
304 to Mineralogy and Petrology, v. 150, p. 268–286.
305 He, W.Y., Yang, L.Q., Brugger, J., McCuaig, T.C., Lu, Y.J., Bao, X.S., Gao, X.Q., Lu, Y.G., and
306 Xing, Y.L., 2017, Hydrothermal evolution and ore genesis of the Beiya giant Au
307 polymetallic deposit, western Yunnan, China: Evidence from fluid inclusions and H – O–S–
308 Pb isotopes: Ore Geology Reviews, v. 90, p. 847–862.
309 Hochella, M.F., Lower, S.K., Maurice, P.A., Penn, R.L., Sahai, N., Sparks, D.L., and Twining,
310 B.S., 2008, Nanominerals, mineral nanoparticles, and earth systems: Science, v. 319, p.
311 1631–1635.
312 Hough, R.M., Noble, R.R.P., and Reich, M., 2011, Natural gold nanoparticles: Ore Geology
313 Reviews, v. 42, p. 55–61.
314 Hu, H., Lentz, D., Li, J.W., McCarron, T., Zhao, X.F., and Hall, D., 2015, Reequilibration
315 processes in magnetite from iron skarn deposits: Economic Geology, v. 110, p. 1–8.
316 Jia, B.P., and Gao, L., 2008, Morphological transformation of Fe_3O_4 spherical aggregates from
317 solid to hollow and their self-assembly under an external magnetic field: The Journal of
318 Physical Chemistry C, v. 112, p. 666–671.

319 Kusebauch, C., Gleeson, S.A., and Oelze, M., 2019, Coupled partitioning of Au and As into
320 pyrite controls formation of giant Au deposits: Science Advances, v. 5, p. eaav5891.
321 Large, R.R., Maslennikov, V.V., Robert, F., Danyushevsky, L.V., and Chang, Z., 2007,
322 Multistage sedimentary and metamorphic origin of pyrite and gold in the giant Sukhoi Log
323 deposit, Lena gold province, Russia: Economic Geology, v. 102, p. 1233–1267.
324 Mao, J.W., Zhou, Y.M., Liu, H., Zhang, C.Q., Fu, D.G., and Liu, B., 2017, Metallogenic setting
325 and ore genetic model for the Beiya porphyry-skarn polymetallic Au orefield, western
326 Yunnan, China: Ore Geology Reviews, v. 86, p. 21–34.
327 Okamoto, H., and Massalski, T.B., 1983, The Au-Bi (gold-bismuth) system: Bulletin of Alloy
328 Phase Diagrams, v. 4, p. 401–407.
329 Palenik, C.S., Utsunomiya, S., Reich, M., Kesler, S.E., Wang, L., and Ewing, R.C., 2004,
330 “Invisible” gold revealed: Direct imaging of gold nanoparticles in a Carlin-type deposit:
331 American Mineralogist, v. 89, p. 1359–1366.
332 Petrella, L., Thébaud, N., Fougerouse, D., Evans, K., Quadir, Z., and Laflamme, C., 2020,
333 Colloidal gold transport: a key to high-grade gold mineralization? Mineralium Deposita,
334 https://doi.org/10.1007/s00126-020-00965-x.
335 Putnis, A., 2002, Mineral replacement reactions: from macroscopic observations to microscopic
336 mechanisms: Mineralogical Magazine, v. 66, p. 689–708.
337 Reich, M., Kesler, S.E., Utsunomiya, S., Palenik, C.S., Chryssoulis, S.L., and Ewing, R.C., 2005,
338 Solubility of gold in arsenian pyrite: Geochimica et Cosmochimica Acta, v. 69, p. 2781–
339 2796.
340 Reich, M., Utsunomiya, S., Kesler, S.E., Wang, L., Ewing, R.C., and Becker, U., 2006, Thermal
341 behavior of metal nanoparticles in geologic materials: Geology, v. 34, p. 1033–1036.

342 Ruiz-Agudo, E., Putnis, C.V., and Putnis, A., 2014, Coupled dissolution and precipitation at
343 mineral–fluid interfaces: Chemical Geology, v. 383, p. 132–146.
344 Sayab, M., Suuronen, J.P., Molnár, F., Villanova, J., Kallonen, A., O Brien, H., Lahtinen, R., and
345 Lehtonen, M., 2016, Three-dimensional textural and quantitative analyses of orogenic gold
346 at the nanoscale: Geology, v. 44, p. 739–742.
347 Scherer, G.W., 1999, Crystallization in pores: Cement and Concrete Research, v. 29, p. 1347–
348 1358.
349 Simon, G., Huang, H., Penner-Hahn, J.E., Kesler, S.E., and Kao, L., 1999a, Oxidation state of
350 gold and arsenic in gold-bearing arsenian pyrite: American Mineralogist, v. 84, p. 1071–
351 1079.
352 Simon, G., Kesler, S.E., and Chryssoulis, S., 1999b, Geochemistry and textures of gold-bearing
353 arsenian pyrite, Twin Creeks, Nevada; implications for deposition of gold in carlin-type
354 deposits: Economic Geology, v. 94, p. 405–421.
355 Seo, J.H., Guillong, M., and Heinrich, C.A., 2009, The role of sulfur in the formation of
356 magmatic–hydrothermal copper–gold deposits: Earth and Planetary Science Letters, v. 282,
357 p. 323–328.
358 Sung, Y.H., Brugger, J., Ciobanu, C.L., Pring, A., Skinner, W., and Nugus, M., 2009, Invisible
359 gold in arsenian pyrite and arsenopyrite from a multistage Archaean gold deposit: Sunrise
360 Dam, Eastern Goldfields Province, Western Australia: Mineralium Deposita, v. 44, p. 765–
361 791.
362 Tooth, B., Brugger, J., Ciobanu, C., and Liu, W.H., 2008, Modeling of gold scavenging by
363 bismuth melts coexisting with hydrothermal fluids: Geology, v. 36, p. 815–818.

364 Tooth, B., Ciobanu, C.L., Green, L., O Neill, B., and Brugger, J., 2011, Bi-melt formation and
365 gold scavenging from hydrothermal fluids: An experimental study: Geochimica et
366 Cosmochimica Acta, v. 75, p. 5423–5443.
367 Williams-Jones, A.E., Bowell, R.J., and Migdisov, A.A., 2009, Gold in solution: Elements, v. 5,
368 p. 281–287.
369 Wirth, R., 2004, Focused Ion Beam (FIB): A novel technology for advanced application of
370 micro- and nanoanalysis in geosciences and applied mineralogy: European Journal of
371 Mineralogy, v. 16, p. 863–876.
372 Wirth, R., 2009, Focused Ion Beam (FIB) combined with SEM and TEM: Advanced analytical
373 tools for studies of chemical composition, microstructure and crystal structure in
374 geomaterials on a nanometre scale: Chemical Geology, v. 261, p. 217–229.
375 Wu, Y.F., Fougerouse, D., Evans, K., Reddy, S.M., Saxey, D.W., Guagliardo, P., and Li, J.W.,
376 2019, Gold, arsenic, and copper zoning in pyrite: A record of fluid chemistry and growth
377 kinetics: Geology, v. 47, p. 641–644.
378 Xing, Y.L., Brugger, J., Tomkins, A., and Shvarov, Y., 2019, Arsenic evolution as a tool for
379 understanding formation of pyritic gold ores: Geology, v. 47, p. 335–338.
380 Yin, S., Wirth, R., Ma, C.Q., and Xu, J.N., 2019, The role of mineral nanoparticles at a fluid-
381 magnetite interface: Implications for trace-element uptake in hydrothermal systems:
382 American Mineralogist, v. 104, p. 1180–1188.
383 Zheleva, T., Jagannadham, K., and Narayan, J., 1994, Epitaxial growth in large-lattice-mismatch
384 systems: Journal of Applied Physics, v. 75, p. 860–871.

Zhou, H.Y., Sun, X.M., Fu, Y., Lin, H., and Jiang, L.Y., 2016, Mineralogy and mineral chemistry of Bi-minerals: Constraints on ore genesis of the Beiya giant porphyry-skarn gold deposit, southwestern China: Ore Geology Reviews, v. 79, p. 408–424.

Zhou, H.Y., Sun, X.M., Cook, N.J., Lin, H., Fu, Y., Zhong, R.C., and Brugger, J., 2017, Nano- to micron-scale particulate gold hosted by magnetite: A product of gold scavenging by bismuth melts: Economic Geology, v. 112, p. 993–1010.

Zhou, H.Y., Sun, X.M., Wu, Z.W., and Huang, Q., 2019, Timing of skarn gold deposition in the giant Beiya polymetallic gold deposit, southwest China: Constraints from in situ monazite SIMS U-Th-Pb geochronology: Ore Geology Reviews, v. 106, p. 226–237.

FIGURE CAPTIONS

FIGURE 1. (a) Simplified geological map of Southwest China. (b) Geological map of the Beiya deposit (after He et al., 2017) and locations of investigated samples and drill core.

FIGURE 2. (a–c) BSE images showing porous low-Si magnetite (Mt) occurring as irregular domains within or penetrating euhedral, non-porous silician magnetite (Si-Mt). The former is of higher BSE intensities and rich in two types of nanoparticle clusters: 1) gold nanoparticles and 2) assemblages of gold, native bismuth (Bi) and bismuthinite (Bis). Note the oscillatory zonation in silician magnetite in (a). (d, e) HAADF images of a FIB foil (location marked in Fig. 2b) showing the association of gold and nanopores (NP) with low-Si magnetite. EDX line scan (white solid line) across the contact zone in (e) displaying large variations in Si contents. (f) BF image across the contact of two types of magnetite illustrating a topotactic reaction.

FIGURE 3. (a) BSE image showing silician magnetite (Si-Mt) replaced by low-Si magnetite (Mt) that is rich in assemblages of gold, native bismuth (Bi) and Bi-Pb-S. (b) HAADF image and EDX spectra of two magnetite types in a FIB foil (location marked in Fig. 3a) showing abundant

nanoparticles of gold, native bismuth and galenobismutite (Gnb) in low-Si magnetite. (c) Representative EDX spectrum of the nanoparticles of the Au and Bi phases in low-Si magnetite.

FIGURE 4. (a, b) BF images showing the (locally) high porosity in low-Si magnetite (Mt). Note that the mean size of nanopores (P) in the upper-left part in (a) is 5 nm (n = 1241) and some nanopores show negative crystals (NC) with rhombic shapes. Other abbreviations: Gnb = galenobismutite. (c) HAADF images of a FIB foil showing low-Si magnetite contacting with silician magnetite (Si-Mt). Note that there are few nanopores and no Au nanoparticle in low-Si magnetite.

FIGURE 5. (a) SEM images of a cubic volume of gold-rich (the bright spots) low-Si magnetite that was FIB-sliced for 3D SEM tomography. (b) 3D rendering illustrating association of gold and nanopores in low-Si magnetite. (c) Examples of gold nanoparticles attached to interconnected nanopores.

FIGURE 6. (a–d) HAADF images showing gold nanoparticles and nanopores (P) in low-Si magnetite (Mt). Note that the EDX spectra of the nanopores are showed at the top-right in (c) and (d). (e) BF image of nanopore-attached gold nanoparticles. (f, g) BF images showing elongate gold nanoparticles along the low-angle boundaries and spheroidal gold nanoparticles within magnetite sub-grains. (h, i) HRTEM images showing interfaces of the elongate (h) and spheroidal (i) gold nanoparticles with low-Si magnetite. The FFT is inserted at the bottom-left.

FIGURE 7. (a–c) HAADF images of nanometer-sized blebs of gold + native bismuth (Bi) and EDX spectrum of Bi-Pb-Ag sulfosalts. Note the overwhelming amounts of Bi-Pb-Ag sulfosalts in the low-Si magnetite and the sharp contacts between gold and native bismuth. (d) BF image of maldonite (Mld) + native bismuth bleb attached to a nanopore (P) and altered by galenobismutite

(Gnb) in low-Si magnetite (Mt). (e–g) HRTEM images and FFT of gold + native bismuth, maldonite and galenobismutite in low-Si magnetite.

FIGURE 8. Binary Au-Bi phase diagram illustrating the solubility of Au in Bi melt as well as eutectics from Au-Bi system (after Okamoto and Massalski, 1983).

FIGURE 9. Schematic illustration of gold nanoparticle formation at mineral-fluid interfaces. (a) Crystallization of silician magnetite from fluids that carried nano-sized Au-Bi melts. (b) CDRR on silician magnetite surfaces forming porous low-Si magnetite and causing the disequilibrium of Au-Bi melts that formed Au-supersaturated fluids at the pore-scale. (c) Heteroepitaxial and randomly-oriented growth of gold nanoparticles in nanopores of low-Si magnetite.

VIDEO CAPTIONS

VIDEO 1. 3D morphology of nanopores in low-Si magnetite.

VIDEO 2. 3D morphology of gold nanoparticles in low-Si magnetite.

VIDEO 3. 3D distribution of gold nanoparticles and nanopores in low-Si magnetite.

Figure 1

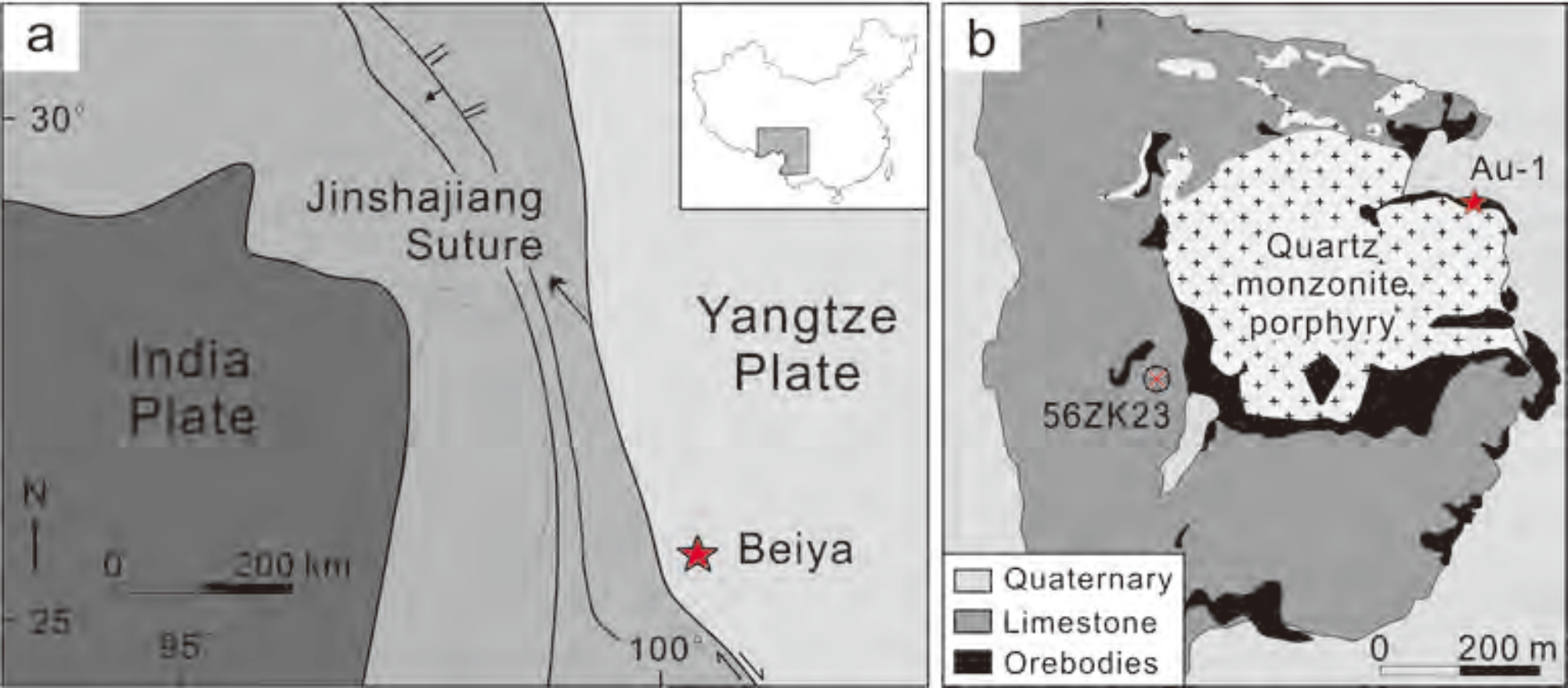
a
30°
Jinshajiang
Suture
India
Plate
Yangtze
Plate
Beiya
N
0
200 km
25
95
100°
b
Au-1
Quartz
monzonite
porphyry
56ZK23
Quaternary
Limestone
Orebodies
0
200 m

Figure 2

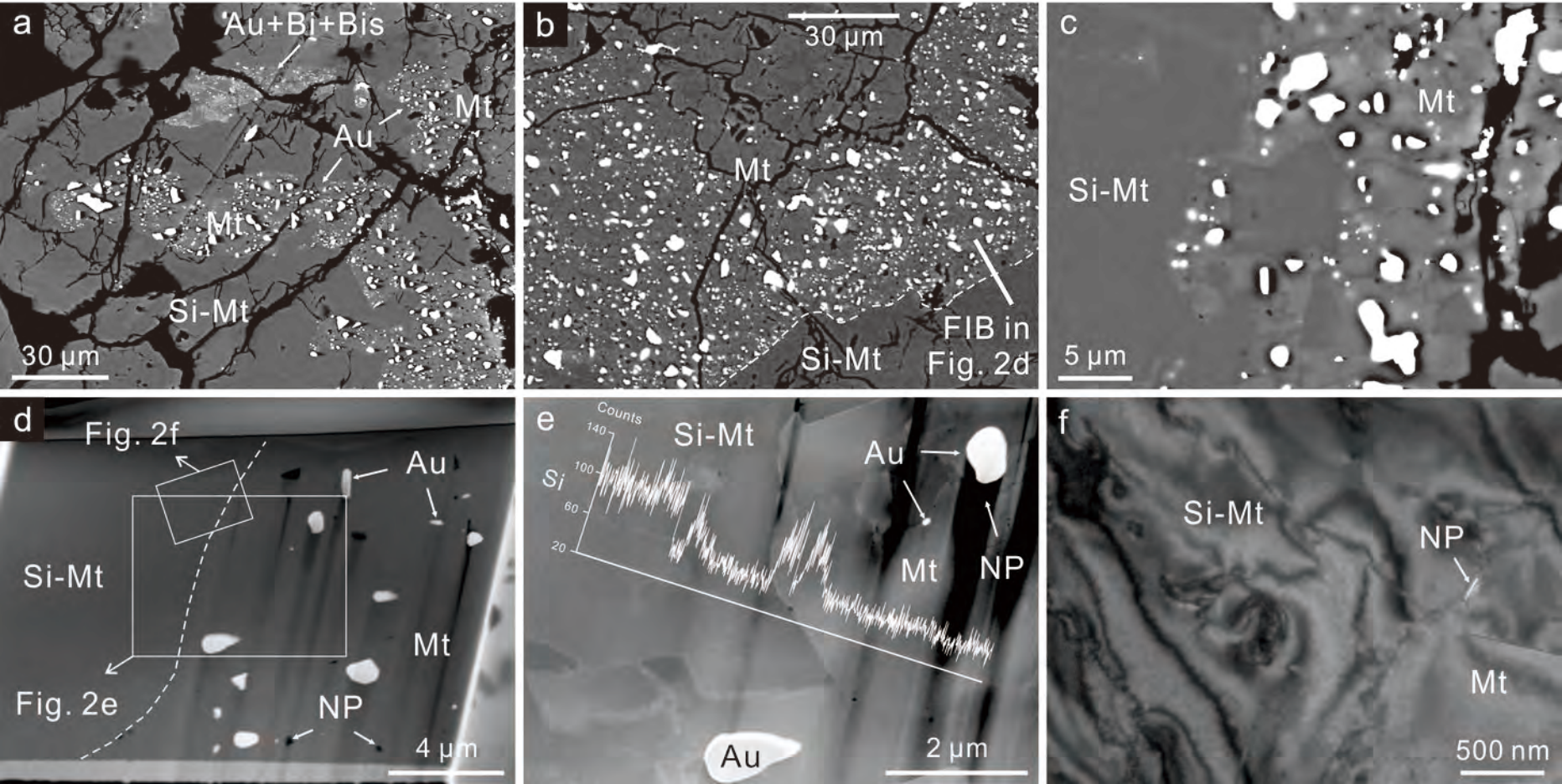
a
Au+Bi+Bis
Mt
Au
Mt
Si-Mt
30 µm
b
30 µm
Mt
Si-Mt
FIB in
Fig. 2d
c
Mt
Si-Mt
5 µm
d
Fig. 2f
Au
Si-Mt
Mt
Fig. 2e
NP
4 µm
e
Counts
140
100
60
20
Si
Si-Mt
Au
Mt
NP
Au
2 µm
f
Si-Mt
NP
Mt
500 nm

Figure 3

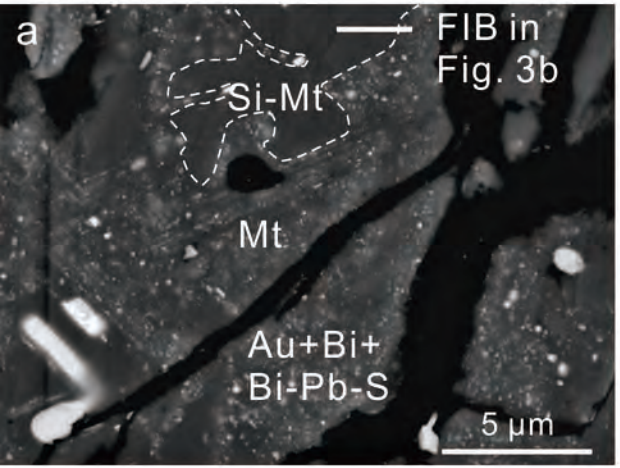
a
FIB in
Fig. 3b
Si-Mt
Mt
Au+Bi+
Bi-Pb-S
5 μm

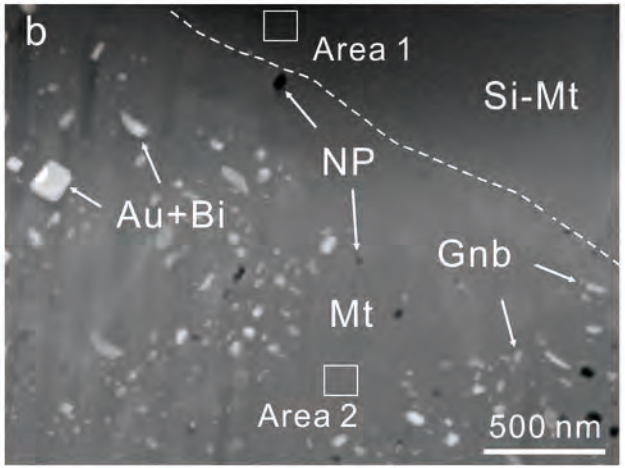
b
Area 1
Si-Mt
NP
Au+Bi
Gnb
Mt
Area 2
500 nm

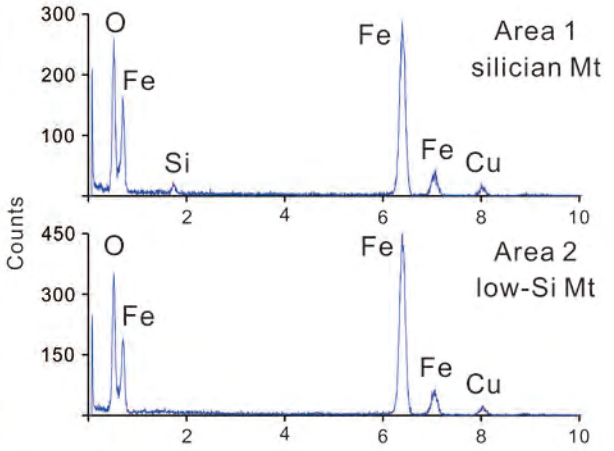
Area 1
silician Mt
Area 2
low-Si Mt
Counts
O
Fe
Si
Cu

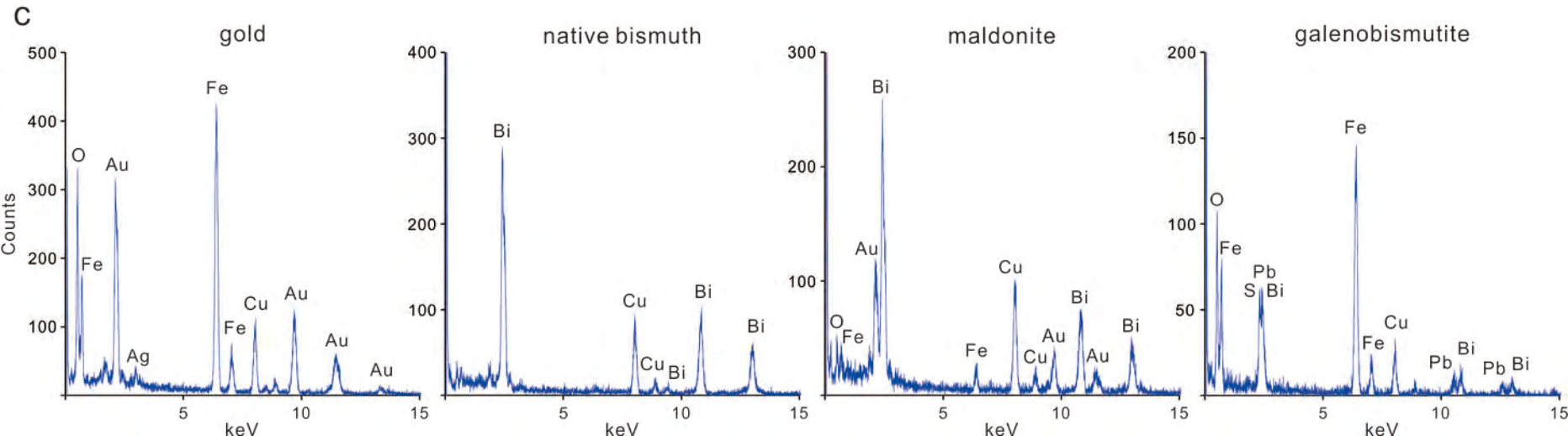
c
gold
native bismuth
maldonite
galenobismutite
Counts
keV
O
Fe
Au
Ag
Cu
Bi
Pb
S

Figure 4

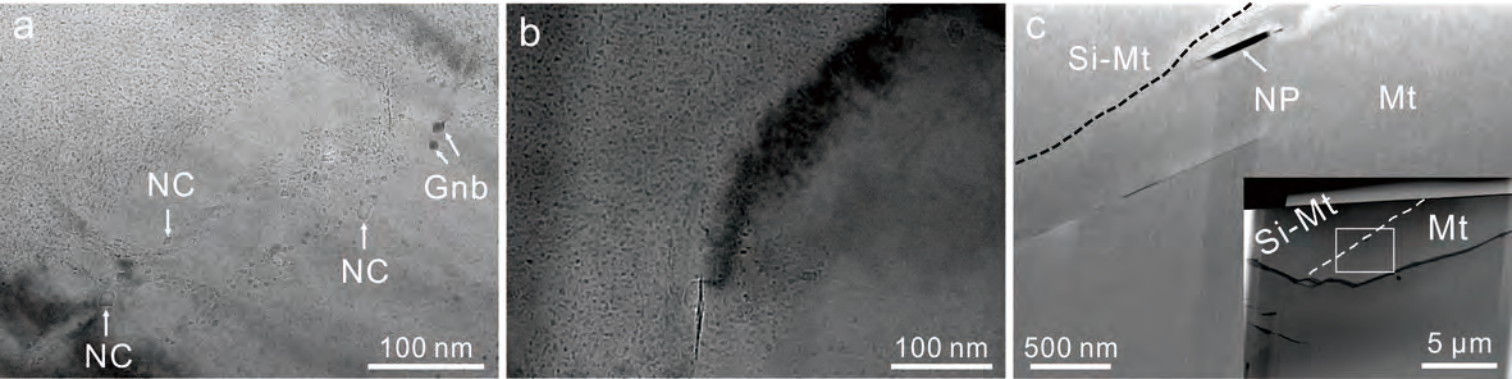

Figure 5

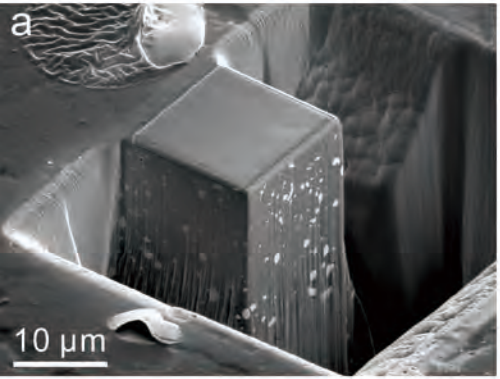

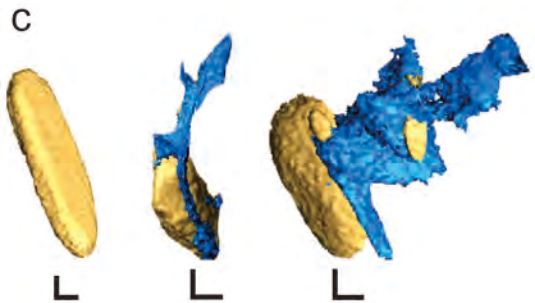

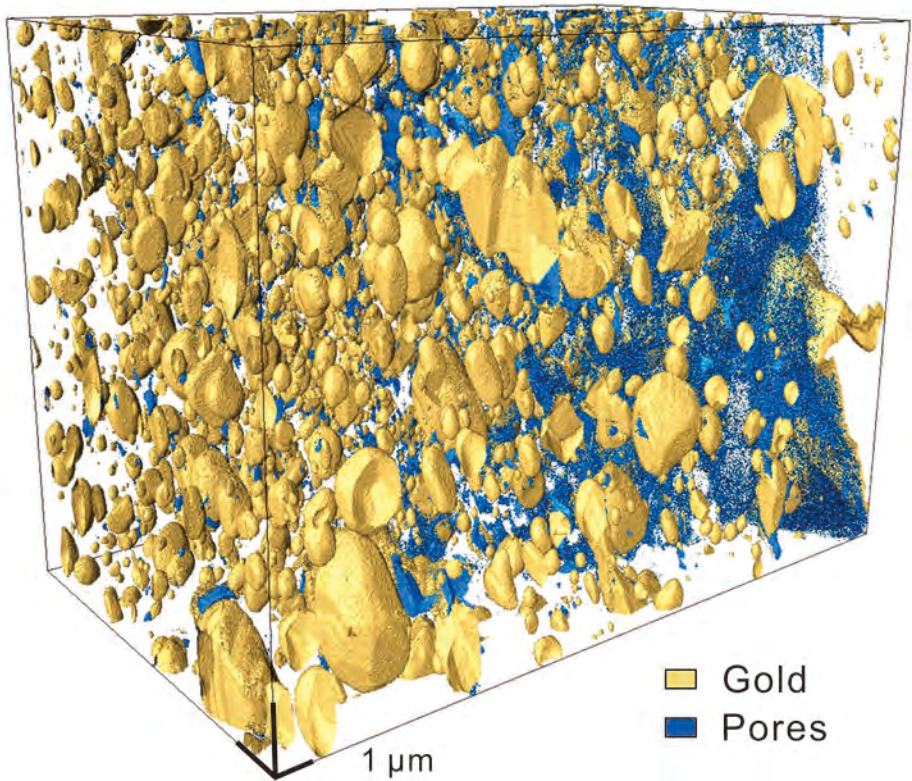

Figure 6

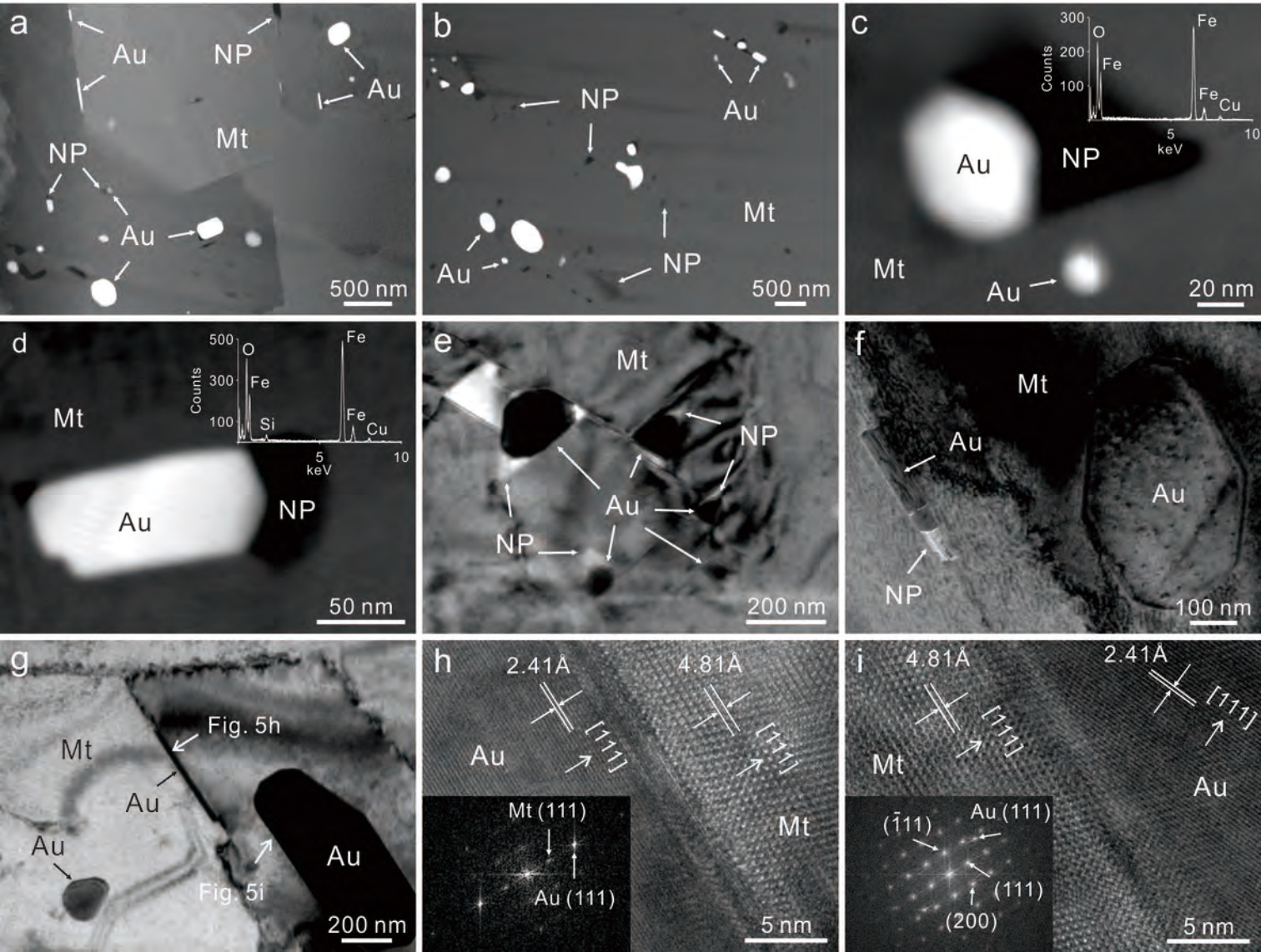
a
Au
NP
Au
Mt
NP
Au
500 nm
b
NP
Au
Mt
Au
NP
500 nm
c
Au
NP
Mt
Au
20 nm
Counts
O
Fe
Fe
Fe
Cu
keV
d
Mt
Au
NP
50 nm
Si
e
Mt
NP
Au
NP
200 nm
f
Mt
Au
Au
NP
100 nm
g
Mt
Fig. 5h
Au
Au
Au
Fig. 5i
200 nm
h
2.41Å
4.81Å
Au
[111]
[111]
Mt
Mt (111)
Au (111)
5 nm
i
4.81Å
2.41Å
[111]
[111]
Mt
Au
(1̄11)
Au (111)
(111)
(200)
5 nm

Figure 7

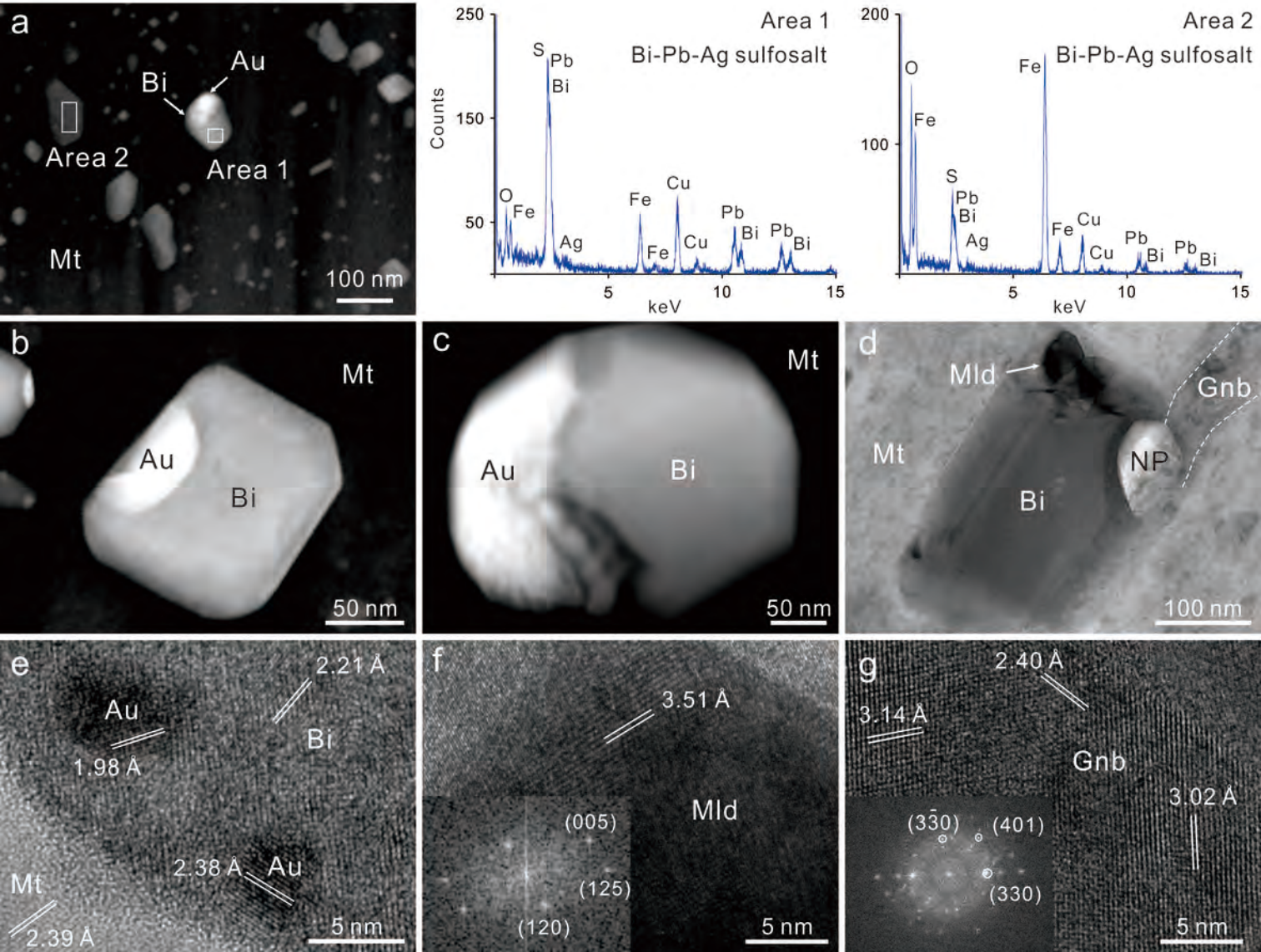
a
Au
Bi
Area 2
Area 1
Mt
100 nm
Area 1
Bi-Pb-Ag sulfosalt
Counts
keV
Area 2
Bi-Pb-Ag sulfosalt
b
Mt
Au
Bi
50 nm
c
Mt
Au
Bi
50 nm
d
Mld
Gnb
Mt
NP
Bi
100 nm
e
2.21 Å
Au
Bi
1.98 Å
2.38 Å
Au
Mt
2.39 Å
5 nm
f
3.51 Å
Mld
(005)
(125)
(120)
5 nm
g
2.40 Å
3.14 Å
Gnb
3.02 Å
(33̄0)
(401)
(330)
5 nm

Figure 8

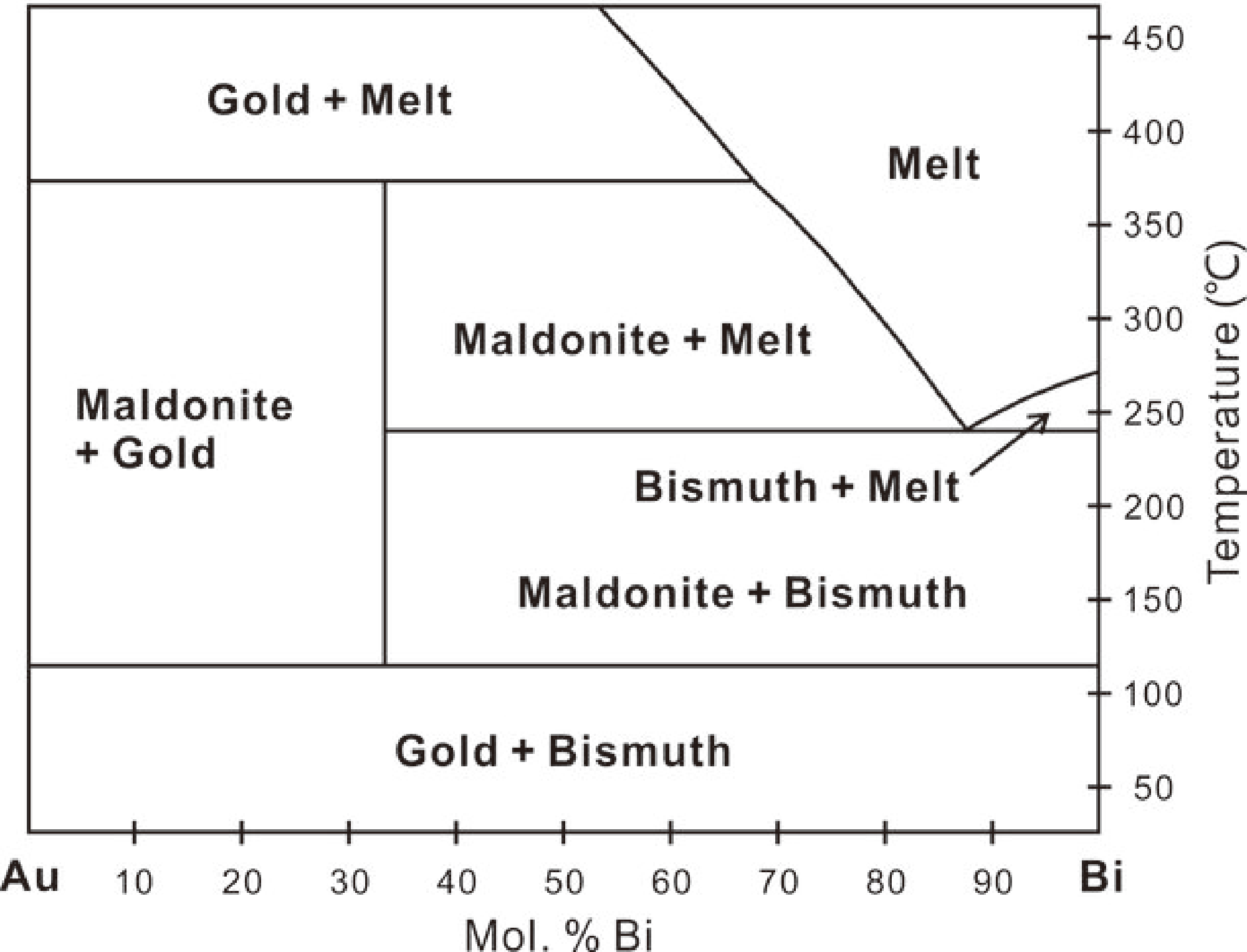
Gold + Melt
Melt
Maldonite + Melt
Maldonite
+ Gold
Bismuth + Melt
Maldonite + Bismuth
Gold + Bismuth
450
400
350
300
250
200
150
100
50
Temperature (°C)
Au
10
20
30
40
50
60
70
80
90
Bi
Mol. % Bi

Figure 9

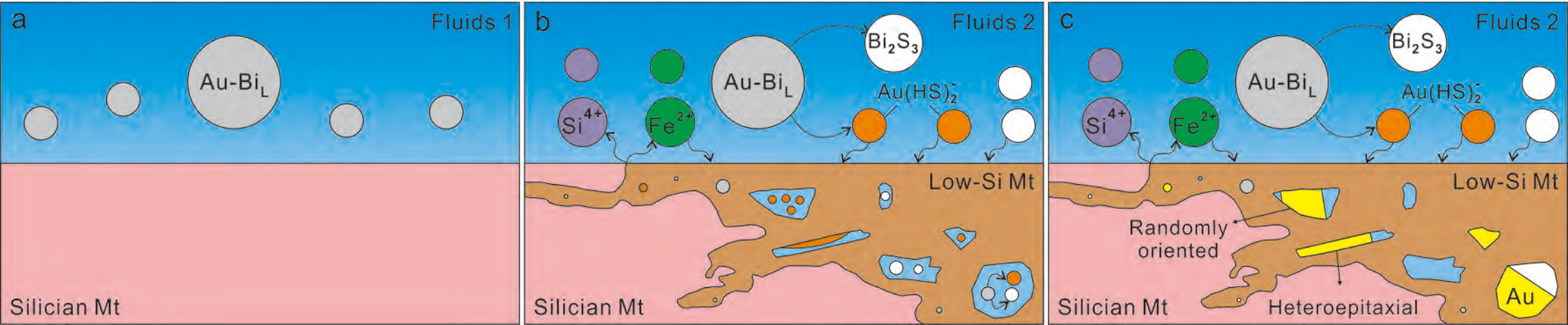
a
Fluids 1
Au-Bi$_L$
Silician Mt
b
Fluids 2
Bi$_2$S$_3$
Au-Bi$_L$
Au(HS)$_2^-$
Si^{4+}
Fe^{2+}
Low-Si Mt
Silician Mt
c
Fluids 2
Bi$_2$S$_3$
Au-Bi$_L$
Au(HS)$_2^-$
Si^{4+}
Fe^{2+}
Low-Si Mt
Randomly oriented
Heteroepitaxial
Au
Silician Mt